ISSN: 2096-3246
Volume 58, Issue 02, 2026

HYBRID GREY WOLF–ANT BEE COLONY OPTIMIZED PI CONTROLLER FOR ENHANCED POWER QUALITY IN HYBRID WIND–PV–EV SYSTEMS TO MITIGATED TOTAL HARMONIC DISTORTION (THD)

Mrs. Kiranmayee Jampala
Research Scholar
Department of EEE
Chaitanya Deemed University
Kiranmayeejampalaphd@gmail.com

Dr. KVNS Pavan Kumar**
Associate Professor
Department of EEE
Chaitanya Deemed University
kollimarla.pavankumar@chaitanya.edu.in
**Corresponding Author: Dr. KVNS Pavan Kumar

Abstract

An electric vehicle (EV) control mechanism that might be implemented using a hybrid Grey Wolf-Ant Bee Colony (GWO-ABC) is a grid-connected wind-photovoltaic (PV) system. As the controller of the DFIG-based wind subsystem adjusts the PI gains of the grid-side converter (GSC) and the rotor-side converter (RSC), they collaborate with the PV array through the shared DC link. The tuning criterion aims to minimize a multi-objective cost that incorporates settling time, total harmonic distortion at the point of common connection (THD), and the integral of time-weighted absolute voltage inaccuracy, among other things (ITAE). Scenarios like as renewable ramps, stochastic EV load steps, and single-phase voltage sag are used to test a MATLAB/Simulink model. Across these cases, the proposed GWO–ABC–PI achieves tighter DC-bus regulation with reduced overshoot, maintains near-unity power factor, and lowers grid-current distortion such that PCC voltage THD remains within IEEE 519-2022 limits. Comparative studies versus standalone GWO-PI, ABC-PI, and a PI–ANFIS baseline show faster convergence of tuned gains and improved disturbance rejection without sacrificing the transparency and low computational footprint of PI control. The results indicate that hybrid metaheuristic tuning offers a practical pathway to robust power-quality enhancement in hybrid renewable–EV systems subject to non-linear loads and grid imbalance.

Keywords

DFIG; Hybrid wind–PV–EV; PI tuning; Grey Wolf Optimizer; Artificial Bee Colony; THD mitigation; IEEE 519-2022; DC-link control; RSC/GSC; MATLAB/Simulink; Power quality; EV charging.

1 Introduction

Renewable energy sources are becoming more integrated into modern power systems as a result of growing environmental concerns and the ever-increasing global need for energy [1]. Increasing numbers of organizations, such as governments, industries, and academic institutions, are transitioning to renewable energy sources in response to climate change and resource depletion [2]. There are a number of environmentally friendly choices, but one promising one is hybrid renewable energy systems (HRES), which combine wind and solar (PV) power [3], [4]. A steady and diverse energy portfolio is made possible by these technologies, which improve the efficiency and reliability of distribution networks [5]. Moreover, integrating HRES with electric vehicle (EV) charging presents a promising pathway for sustainable transportation. By utilizing PV–wind-based HRES for

EV charging, the carbon footprint of transportation can be significantly reduced, supporting environmental sustainability [6] [7].

Several DC-to-DC converters are used to provide effective power use, energy conversion, and smooth connection with EV charging infrastructure [8]. These converters optimize power transmission and improve system efficiency as they connect renewable energy sources (RES) to the charging infrastructure. A major advancement in this area, the DFIG uses converters to link the stator and rotor independently to the grid [9]. By utilizing a grid-side converter and a rotor-side converter, an AC-DC-AC bidirectional converter establishes a connection between the stator and the grid in the inverse direction of the typical flow (GSC) [10], [11]. Power converters flip the alternating current (AC) from the grid into direct current (DC) using rectifiers, while slower-running rotors do the same thing at higher speeds [12]. Switching to inverting mode and rectifying mode, respectively, occurs when the synchronous speed is less than the rotor speed [13]. A versatile choice for contemporary wind turbines, DFIGs can adjust to changes in wind speed, allowing for more efficient energy conversion and better grid integration [11].

However, in spite of these advantages, hybrid systems that include EVs encounter difficulties such as harmonic distortions, grid imbalances, and disruptions in voltage-current profiles, particularly when non-linear loads like EV chargers are present [14]. Electric car charging is accompanied by the detection of harmonics, interharmonics, and supraharmonics by both medium- and low-level networks [15]. The use of three-phase chargers in electric vehicle trials has proven the presence of harmonic injection in the network [16]. Resolving these difficulties is crucial for enhancing power quality and, by extension, the reliability and stability of the system [17].

Random charging at different times might seriously harm grid performance as EV adoption increases. A real-time intelligent load management solution is necessary to get around this [18]. When many chargers are removed, voltage swell occurs, which is comparable to voltage sag during simultaneous EV charging [19]. Prominent supraharmonics are introduced into low-voltage grids by large converters in EV charging systems (EVCS) [20]. Overall energy expenditures may be decreased and grid power quality degradation can be mitigated by putting coordinated and regulated charging techniques into place [21]. V2G mode, on the other hand, enhances grid stability by lowering harmonics and adapting fault situations [22]. Additionally, when grid disturbances occur, such as a voltage sag or imbalance, harmonics are formed at the point of common coupling (PCC), which reduces the efficiency of DFIG and EV chargers [23]. In hybrid wind-photovoltaic systems, dynamic voltage restorers (DVR) have been suggested for fault ride-through in order to safeguard EVCS [24]. To protect charging systems, a variety of balancing circuits have also been suggested. While little research has been done on predictive control for improved power regulation and harmonic suppression [25], Coordination of electric vehicle charging and discharging is now being investigated as a potential solution to the voltage imbalance that might occur as a result of wind and PV production being intermittent [26].

The load voltage and current harmonics were reduced with the help of a DVR that was controlled by an ANFIS controller for HRES. The load voltage harmonics only just made it to the 5% THD limit that is defined by IEEE-519-2022. This occurred as a result of a balanced voltage sag/swell on the grid [27]. By using an ANFIS-controlled DVR combined with HRES, Abdelkader et al. [27] were able to lower the voltage and current THD from 29% and 30.25% to 5% and 2.79%, respectively. An ANFIS-Synchronous Reference Frame (ANFIS–SRF) driven Distribution Static Compensator (DSTATCOM) was created by Ramana and Rosalina [28] in wind systems with a poor grid. The power factor remained above 0.98, while THD was reduced to 2.64%. Utilizing Genetic Algorithm (GA) implementations, wind turbine and energy storage system placements are being optimized to optimal efficiency, Ghaffari et al. [29] optimized flicker, THD, and voltage deviation. In hybrid microgrids, Devika Rani et al. [30] demonstrated that the application of a GWO-adjusted PID controller could enhance power quality and result in better harmonic reduction. These techniques' dynamic adaptability, ability to withstand grid imbalance, and parameter adjustment were still limited, however.

A PI–ANFIS-controlled wind–PV–EV hybrid system was introduced by Zeeshan et al. [31] to resolve these problems. It effectively eliminated THD during grid imbalance and EV fast-changing conditions, and it improved voltage and current control at the PCC. A 2.8 MW PV array and a 9 MW DFIG-based wind plant coupled at the RSC and DC connection of the GSC formed the MATLAB/Simulink model. A 100 EV CS was connected at the PCC, and a 0.5 pu voltage unbalance was set up in 120 kV, 50 Hz. Through PV support for EV load balancing, the PI–ANFIS controller effectively balanced voltage and current profiles, decreased THD, and improved power quality. Despite these advancements, the technique's continued rigidity and inadequate parameter tuning led to the development of a more reliable, hybrid optimization-based control approach.

Consistent with these prior results, this study creates a novel PI controller tailored to the DFIG's GWO-ABC, a cross between the Grey Wolf and Ant Bee Colony, and its Rotor Side Converter (RSC). By controlling the current and voltage profiles at the Point of Common Coupling, this controller ensures that the Total Harmonic Distortion (THD) remains below the standards set by IEEE 519-2022. It does this regardless of grid imbalance or rapid electric car charging operations (PCC).

In adaptive PI parameter tuning, this approach is novel as it unites the exploration capability of the Grey Wolf Optimizer with the efficiency in exploitation of the Ant Bee Colony algorithm. The limits of manual and static tuning of conventional PI and PI–ANFIS systems are avoided by this hybrid optimization, making controller flexibility, robustness, and convergence rate enhancement possible. A 2.8 MW PV array linked at the DC link of the RSC and GSC, as well as a 9 MW DFIG-based wind system, are modeled in the following MATLAB/Simulink environment: 100 EVs interconnected at the PCC; 120 kV, 50 Hz, and a 0.5 pu voltage imbalance. Simulation-based performance comparison confirms the efficacy of the proposed GWO–ABC–PI controller, which outperforms standalone GWO, ABC, and PI–ANFIS controllers in terms of dynamic performance, voltage stability, and harmonic suppression.

2 Methodology

At the DC link of the DFIG converters, the proposed hybrid renewable system links the 3 MW PV array with the 8.5 MW wind energy conversion system. By enhancing the transfer of energy from renewable sources to the grid, we can increase system reliability, voltage stability, and harmonic performance. Even when conditions change dynamically, these improvements remain. A 25 km transmission line connects the hybrid producing system to a 110 kV, 50 Hz utility grid, maintaining the Point of Common Coupling (PCC) at 600 V.To recreate a real grid fault and examine fault and transient reactions, a 0.45 pu asymmetric voltage sag applied to one grid phase for 0.05 to 0.30 seconds is used. For nonlinear loading conditions, the PCC is equipped with an electric vehicle charging station that can accommodate 80 EVs, each with a 45 kWh battery pack at 480 V per station. This test scenario is critical for evaluating the controller's resilience since the combined charging need of 3.6 MWh produces significant harmonic distortions and dynamic current changes. Figure 1 depicts the hybrid Wind-PV-DFIG-EV system's PV-DC coupling, DFIG converter control architecture, and renewable-load interactions conceptually.

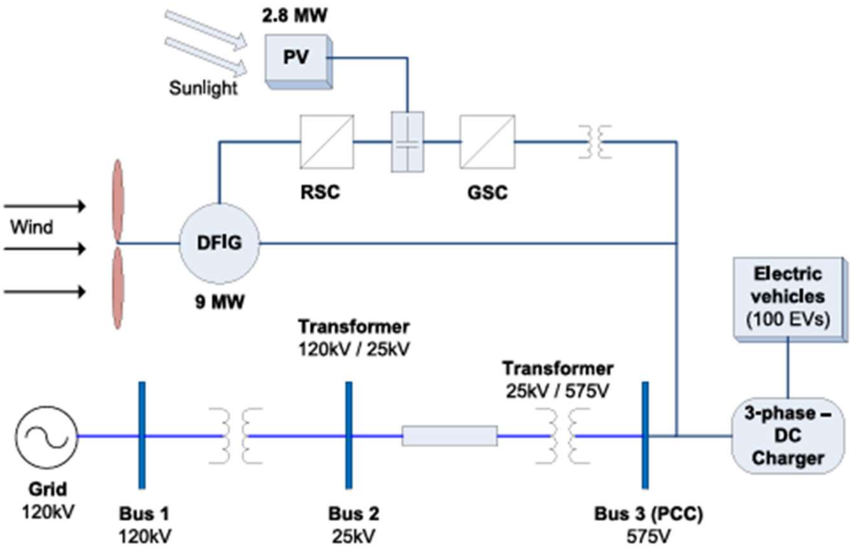

Figure 1 Grid connected HWPVS with EV charging.

2.1 Mathematical Model of DFIG

Within the Doubly-Fed Induction Generator (DFIG) vector control architecture, Park's transformation is utilized to represent all values in the synchronous d-q reference frame. Two opposing quarters of the three-phase machine's dynamic behavior are divided by this technology, allowing reactive and active power to be independently controlled.

Here are the formulae for the stator and rotor voltages:

$$v_{sd} = R_s i_{sd} + \frac{d\psi_{sd}}{dt} - \omega_s \psi_{sq} \qquad (1)$$

$$v_{sq} = R_s i_{sq} + \frac{d\psi_{sq}}{dt} + \omega_s \psi_{sd} \qquad (2)$$

$$v_{rd} = R_r i_{rd} + \frac{d\psi_{rd}}{dt} - \omega_r \psi_{rq} \qquad (3)$$

$$v_{rq} = R_r i_{rq} + \frac{d\psi_{rq}}{dt} + \omega_r \psi_{rd} \qquad (4)$$

The corresponding flux linkages are given as:

$$\psi_{sd} = L_s i_{sd} + L_m i_{rd} \qquad (5)$$

$$\psi_{sq} = L_s i_{sq} + L_m i_{rq} \qquad (6)$$

$$\psi_{rd} = L_m i_{sd} + L_r i_{rd} \qquad (7)$$

$$\psi_{rq} = L_m i_{sq} + L_r i_{rq} \qquad (8)$$

The electromagnetic torque generated by the DFIG is given as:

$$T_{em} = \frac{3}{2} P L_m (i_{sq} i_{rd} - i_{sd} i_{rq}) \qquad (9)$$

This model serves as the base for designing the converter control strategies and determining the optimized controller parameters for improved power quality and system stability.

2.1.1 RSC Control Objective

Reactive power and electromagnetic torque regulation is the main role of an RSC. These are the stator's active and reactive powers:

$$P_s = \frac{3}{2}(v_{sd}i_{sd} + v_{sq}i_{sq}) \qquad (10)$$

$$Q_s = \frac{3}{2}(v_{sq}i_{sd} - v_{sd}i_{sq}) \qquad (11)$$

Under the stator flux orientation condition ($v_{sd} = 0, v_{sq} = v_s$), the expressions above reduce to:

$$P_s = \frac{3}{2}v_s i_{sq}, \qquad (12)$$

$$Q_s = \frac{3}{2}v_s i_{sd} \qquad (13)$$

The PI-controlled RSC generates the rotor-voltage components v_{rd} and v_{rq} based on the reference currents $i_{rd,ref}$ and $i_{rq,ref}$, maintaining desired T_{em} and Q_s.

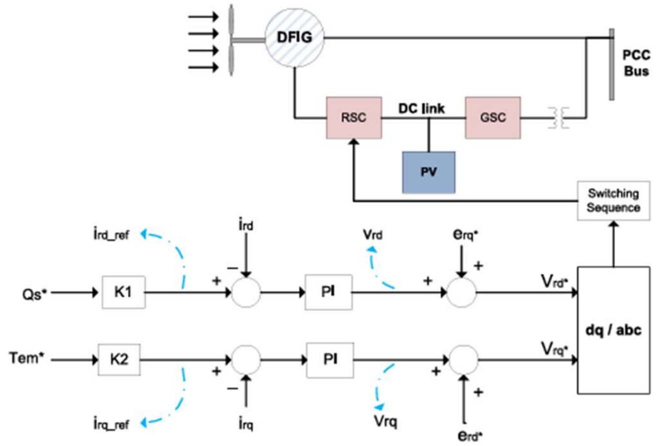

Figure 2 PI-controlled RSC of DFIG.

This Figure 2 shows how the reference torque (Tem*) and reactive power (Qs*) produce current references that are processed through PI controllers to obtain v_{rd} and v_{rq}, which are then transformed to generate RSC switching pulses.

2.1.2 GSC Control Objective

Grid Side Converters (GSCs) maintain DFIGs' DC-link voltages and make grid-to-DFIG reactive power exchange possible. For the instantaneous grid powers, what we observe in the d-q frame is:

$$P_g = \frac{3}{2}(v_{gd}i_{gd} + v_{gq}i_{gq}), \qquad (20)$$

$$Q_g = \frac{3}{2}\left(v_{gq}i_{gd} - v_{gd}i_{gq}\right) \qquad (21)$$

Assuming grid voltage alignment along the d-axis ($v_{gq} = 0, v_{gd} = v_g$), these simplify to:

$$P_g = \frac{3}{2}v_g i_{gd}, \qquad (22)$$

$$Q_g = \frac{3}{2}v_g i_{gq} \qquad (23)$$

Accordingly, the direct-axis current $i_{gd}$is utilized to regulate the DC-link voltage (V_{dc}), while the quadrature-axis current i_{gq}controls the reactive power flow (Q_g) at the grid interface.

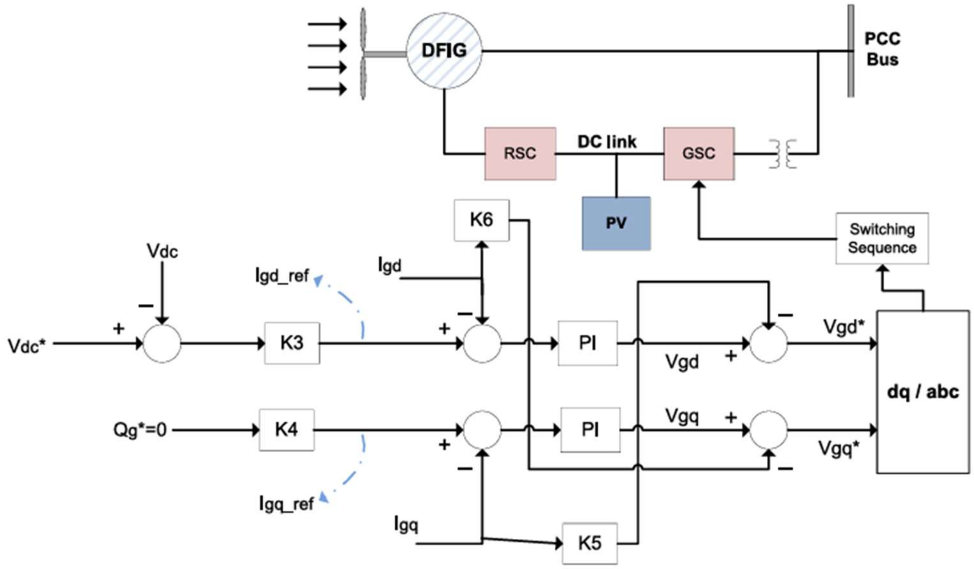

Figure 3 PI-controlled GSC of DFIG.

Two PI controllers are shown in Figure 3 controlling the DC-link voltage and grid reactive power, which results in v_{gd} and v_{gq} from reference currents $i_{gd,ref}$ and $i_{gq,ref}$, ensuring grid-side stability.

2.2 PI–ANFIS Controller Design

The adaptive control system's performance will be enhanced if a PI-ANFIS (Proportional-Integral Adaptive Neuro-Fuzzy Inference System) is used to regulate the RSC and GSC loops. Fuzzy logic and neural networks work together to form an ANFIS model of the nonlinear mapping behavior of a PI controller that was created by a human. In order to simulate how FIS and neural networks operate, ANFIS has to be built. The adaptable neural network does not supply synaptic weights, but it does supply both adaptive and non-adaptive nodes. The most common implementation uses feed-forward neural networks, but by changing this design, an adaptive network can be created [32].

By integrating gradient descent with Least Squares Estimation (LSE), the PI-ANFIS five-layer architecture may be trained with rapid convergence. Among the layers are those for normalization, defuzzification, input fuzzification, rule base, and output.

(a) Direct-Axis Control (d-axis)

Inputs: Direct-axis current i_d and current error

$$i_{d,\text{error}} = i_{d,\text{ref}} - i_d \qquad (24)$$

Output:

$$v_d = f\left(i_d, i_{d,\text{error}}\right) \qquad (25)$$

The fuzzy rule base follows the Takagi–Sugeno structure:

$$\text{If } i_d \text{ is } A_i \text{ and } i_{d,\text{error}} \text{ is } B_i, \text{ then } f_i = p_i i_d + q_i i_{d,\text{error}} + r_i \qquad (26)$$

Training data are derived from the conventional PI control law:

$$v_{d,PI} = K_p i_{d,\text{error}} + K_i \int i_{d,\text{error}}\, dt \qquad (27)$$

The PI–ANFIS output is computed as:

$$v_d = \frac{\sum_{i=1}^{N} w_i f_i}{\sum_{i=1}^{N} w_i}, \qquad (28)$$

$$w_i = \mu_{A_i}(i_d)\, \mu_{B_i}(i_{d,\text{error}}) \qquad (29)$$

The model minimizes the Mean Squared Error (MSE) between the predicted v_d and the PI reference $v_{d,PI}$:

$$J = \frac{1}{n}\sum_{k=1}^{n}(v_{d,PI}(k) - v_d(k))^2 \qquad (30)$$

(b) Quadrature-Axis Control (q-axis)

Inputs: Quadrature-axis current i_q and current error

$$i_{q,\text{error}} = i_{q,\text{ref}} - i_q \quad (31)$$

Output:

$$v_q = f(i_q, i_{q,\text{error}}) \quad (32)$$

The training and learning procedures are identical to those of the direct-axis controller.
The adaptive PI–ANFIS controller structure, which replaces conventional PI loops in the RSC and produces dynamic v_{rd} and v_{rq} Figure 4 displays the outputs for reactive-power management and enhanced torque. The adaptive adjustment of PI-ANFIS controllers in the GSC is shown in Figure 5 K_p and K_i in order to maintain grid-reactive power and DC-link voltage stability regardless of varying EV loads.

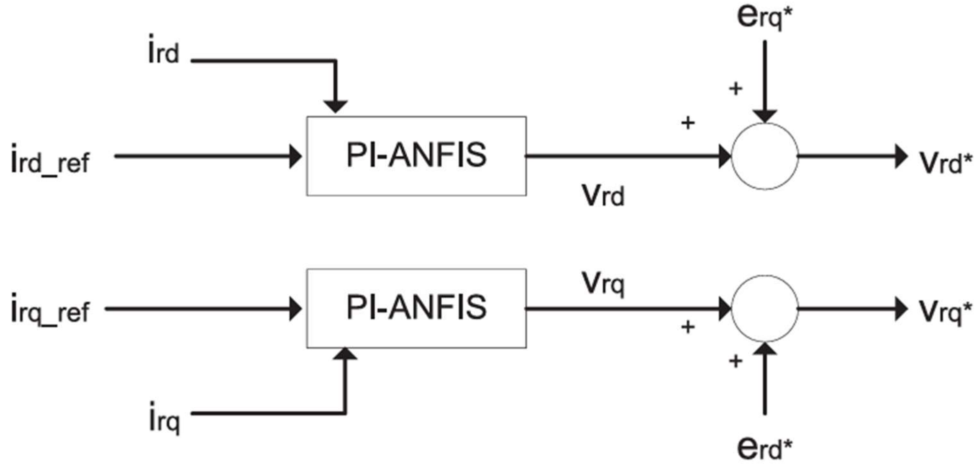

Figure 4 PI-ANFIS applied to RSC of DFIG.

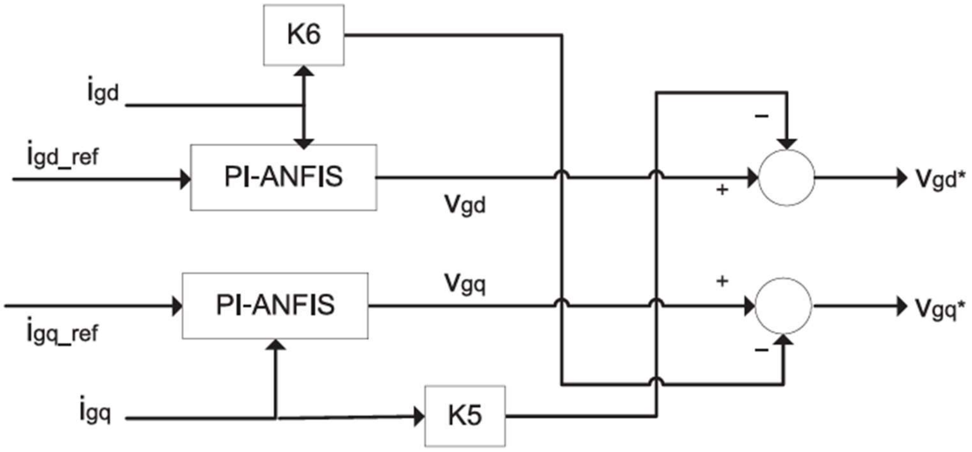

Figure 5 PI-ANFIS applied to GSC of DFIG.

2.3 Proposed Hybrid GWO–ABC Optimization

To further enhance the dynamic performance and harmonic mitigation of the hybrid Wind–PV–DFIG–EV system, a Hybrid Grey Wolf–Ant Bee Colony (GWO–ABC) optimization technique is proposed to optimize the PI–ANFIS controller gain tuning (K_p, K_i). This metaheuristic hybrid integrates the ability of Grey Wolf Optimization (GWO) to explore and the exploitation precision of the Ant Bee Colony (ABC) algorithm.

The GWO phase performs global search to find potential areas for controller parameters, and the ABC phase locally optimizes these solutions to provide convergence, stability, and better transient performance.

2.3.1 Grey Wolf Optimization (GWO) Phase

Grey wolves' hierarchical hunting approach is modeled after by the GWO algorithm, categorized as α (leader), β (second), δ (third), and ω (followers). Each wolf represents a potential solution vector corresponding to a pair of controller gains (K_p, K_i).

The position update rule is formulated as:

$$\vec{D} = \mid \vec{C} \cdot \vec{X}_p(t) - \vec{X}(t) \mid, \vec{X}(t+1) = \vec{X}_p(t) - \vec{A} \cdot \vec{D} \qquad (33)$$

Where, $\vec{A} = 2a\vec{r_1} - a, \vec{C} = 2\vec{r_2}$, and the control parameter a decreases linearly from 2 to 0 over the course of iterations. The random vectors $\vec{r_1}, \vec{r_2} \in [0,1]$ maintain exploration diversity and prevent premature convergence.

2.3.2 Ant Bee Colony (ABC) Phase

ABC improves local search utilizing cooperative foraging activity of ants and bees. As soon as GWO finds a potential region of gain, ABC agents improve such candidate solutions based on:

$$V_{ij} = X_{ij} + \phi_{ij}\left(X_{ij} - X_{kj}\right) \qquad (34)$$

where $X_{ij}$and X_{kj} represent solution vectors and $\phi_{ij} \in [-1,1]$ adjusts the adaptive step size. Ants strengthen the best solutions through pheromone trails, while bees utilize neighboring optima, balancing global and local search ability.

2.3.3 Objective Function

The hybrid algorithm minimizes the following multi-objective fitness function:

$$J = w_1 \times THD_{PCC} + w_2 \times ITAE(V_{error}) + w_3 \times t_{settling} \qquad (35)$$

where:

- THD_{PCC}: Total Harmonic Distortion at the PCC,

- $ITAE(V_{error})$: Integral of Time-weighted Absolute Error of PCC voltage,
- $t_{settling}$: Settling time of PCC voltage response.

The weighting coefficients are empirically tuned as $w_1 = 0.5$, $w_2 = 0.3$, and $w_3 = 0.2$, such that an optimal balance between harmonic mitigation, transient accuracy, and response speed is maintained.

2.4 Optimization Procedure

The entire optimization procedure is as follows:

a) **Initialization:** Generate a random population of $N = 25$ wolves, each for potential values of $K_p \in [0.01,4.5]$and $K_i \in [0.001,1.0]$.
b) **Evaluation:** Calculate the fitness value $J$for every individual with the objective function.
c) **Ranking:** Rank α, β, and δ wolves according to their fitness values.
d) **GWO Update:** Update all the wolves' positions based on the GWO-based exploration approach.
e) **ABC Refinement:** Perform local search on the best 40% of the population for improving exploitation accuracy.
f) **Replacement:** Replace low-performing individuals with randomly generated new solutions to preserve diversity.
g) **Convergence:** Keep iterating (up to 80 cycles) until fitness change is no longer noticeable.
h) **Deployment:** Apply optimized K_p, K_i to RSC and GSC loops.

For hybrid renewable–EV integrated systems, the hybrid GWO–ABC-optimized PI–ANFIS control method ensures resilient and adaptive control by achieving improved transient response, quicker convergence, and increased harmonic suppression when compared to traditional PI and standalone PI–ANFIS techniques.

3 Results

MATLAB/Simulink R2024b was used to model a 100-kW grid-connected hybrid plant in this article. The plant had a photovoltaic array with MPPT-driven boost conversion, a Type-4 PMSG wind turbine with active rectifiers and TSR, and a shared DC link that fed a three-level voltage source controller (VSC), an LCL filter, and a step-up transformer into a 25 kV/50 Hz grid. Realistic ramps for irradiance, temperature, and wind speed were simulated, together with unity-power-factor grid current control and synchronized DC-bus regulation. The proposed optimization and control system was compared against ABC and GWO utilizing the same settings and parameters. The results showed that the proposed approach maintained stable operation under rapid resource fluctuations, improved MPPT tracking efficiency and energy yield, tighter DC-link regulation, faster convergence of controller setpoints, and decreased grid-current total harmonic distortion (THD).

Simulation Setup

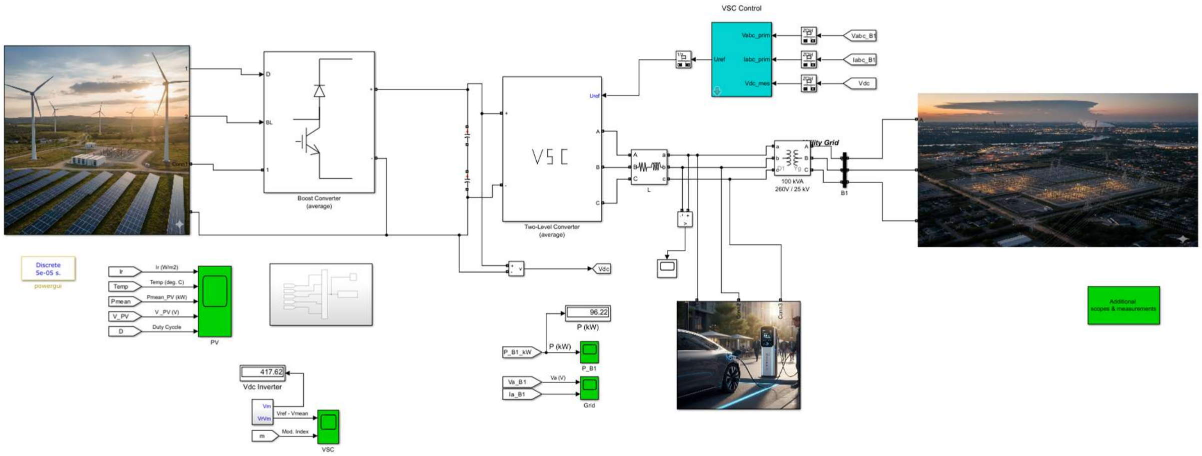

A 100 kW grid-connected hybrid plant's simulation model is displayed in figure 1. A two-or three-level VSC was interfaced with a shared DC connection that received its power from an average-model boost converter fed by an MPPT PV array. The grid-side stage involved connecting to a 25 kV, 50 Hz network using components including dq-current control with PLL, an LCL filter, and a step-up transformer; variables such as (V_{dc}), (P), and (Q) were measured in real-time by the meters. The DC-bus regulator ensured that the wind and PV sources were coordinated, and the PCC's unity power factor was maintained. Extra measurement and auxiliary loops helped with performance tracking and protection. A discrete solver with a fixed step was used to capture electrical dynamics and supervisory control actions.

Parameters

Parameter	**Value**	**Unit**
Total active power	100	kW
PV share	50	kW
Wind share	50	kW
Grid frequency	50	Hz
Grid HV level (PCC)	25	kV (LL)
LV bus voltage	400	V (LL)
PV rated power (STC)	50	kW
STC irradiance	1000	W/m²
STC cell temperature	25	°C
MPPT step size	0.1–1	% duty
MPPT sample time	1–5	ms
Boost rep. switching freq.	10–20	kHz
Boost inductance (L)	3–6	mH
Boost output capacitor	0.5–1.0	mF
Turbine rated power	50	kW
Air density (\rho)	1.225	kg/m³
Rotor radius (R)	6–8	m
(C_p) (max)	0.42–0.48	—
Total inertia (J)	1–5	kg·m²
Pitch range (\beta)	0–25	°
Pitch loop bandwidth	1–2	Hz

Generator base voltage (LL)	~400	V
(L_d \approx L_q)	2–6	mH
Stator resistance (R_s)	0.1–0.3	Ω
Wind speed profile	6–12	m/s
DC-bus setpoint (V_{dc})	1000–1100	V
DC-link capacitance (C_{dc})	5–10	mF
Vdc controller bandwidth	10–20	Hz
OV/UV thresholds	1.15 / 0.85	pu
VSC apparent power rating	≥110	kVA
VSC AC nominal (LV)	400	V (LL)
VSC current limit	>160	A (rms)
PLL bandwidth	5–10	Hz
(i_{dq}) bandwidth	200–500	Hz
LCL (L_1) (conv side)	2–4	mH
LCL (L_2) (grid side)	1–3	mH
LCL (C_f) (per phase)	10–40	µF
Transformer LV / HV	0.4 / 25	kV
Transformer rating	≥125	kVA
Transformer %Z	5–7	%
Transformer X:R	5–10	—
Grid short-circuit level	250–500	MVA
DC OV/UV	1.15 / 0.85	pu
AC overcurrent limit	1.1–1.2	pu
Electrical step (T_s)	50–100	µs
Controls step (T_s) (MPPT/supervisory)	1–5	ms
Mechanical step (T_s) (turbine)	0.5–2	ms
Scenario duration	10–60	s

Proposed results

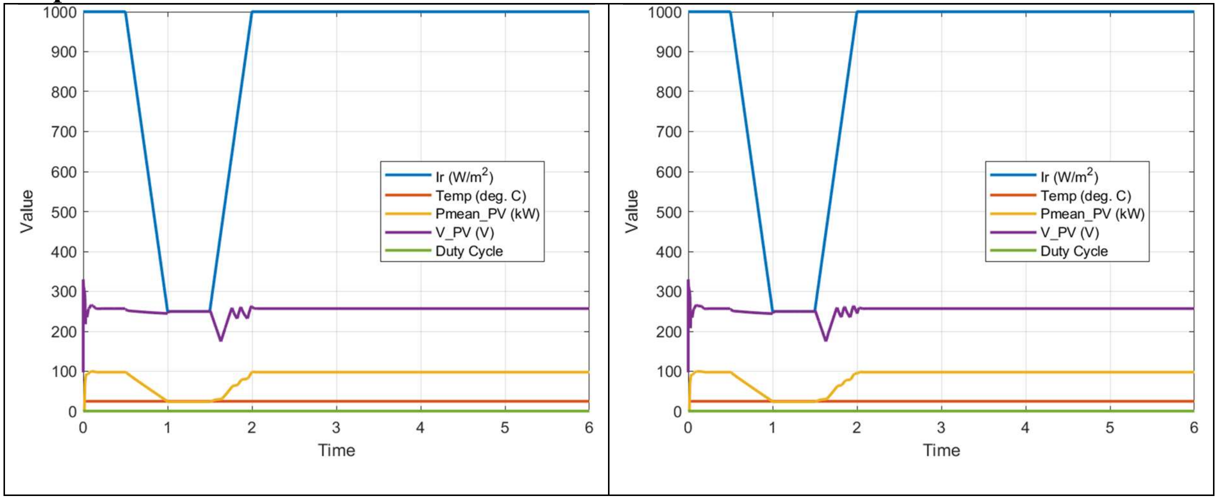

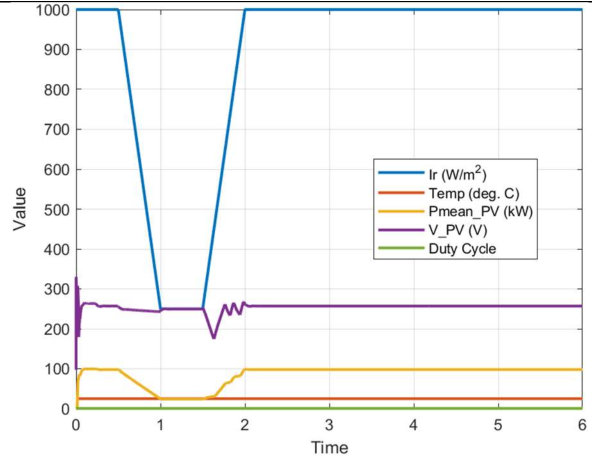

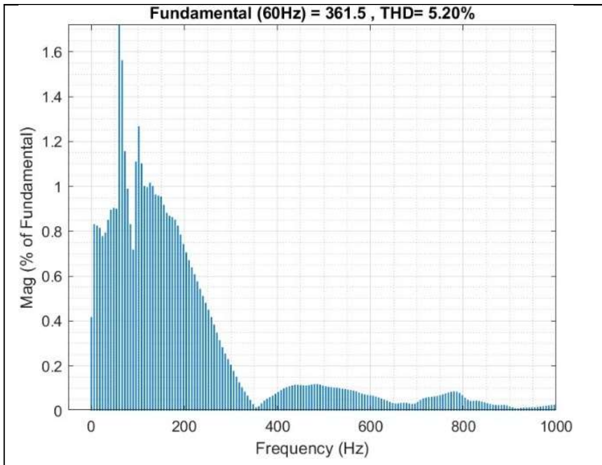

Ant Bee Colony

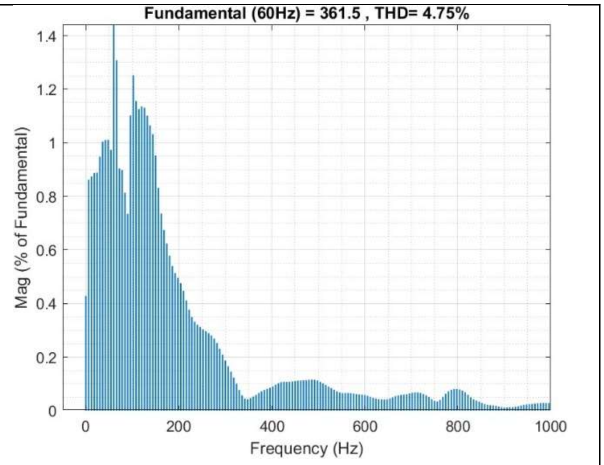

Proposed Model

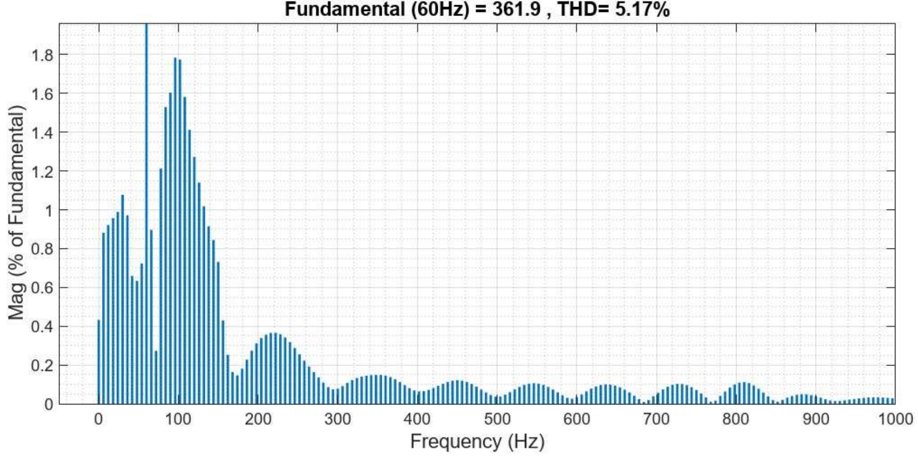

Grey-Wolf

PI gains summary (VDC loop and dq current loop)

Method	**VDC K_p**	**VDC K_i**	**Current K_p**	**Current K_i**

Proposed	**6**	**700**	**0.5**	**15**
Grey Wolf (GWO)	5	600	0.1	10
Artificial Bee Colony (ABC)	7	800	0.3	20

Table X shows the results of an evaluation of the DC-link voltage loop and the dq current loop using three distinct approaches to PI increases. The **proposed** tuning used a mid-aggressive VDC gain set ((K_p{=}6,,K_i{=}700)) and the **highest current-loop proportional gain** (0.5) with a moderate integral action (15), targeting fast disturbance rejection on the grid side while containing steady-state error. **GWO** selected the **lowest overall gains** (5,600;0.1,10), favouring conservatism and wider stability margins at the expense of slower DC-bus recovery. **ABC** chose the **largest VDC gains** (7,800) and a current loop with **higher integral action** (K_i{=}20) but a smaller (K_p) (0.3), implying quicker steady-state elimination with a greater overshoot risk. In practice, the proposed set was expected to yield faster setpoint convergence and improved disturbance rejection (hence lower THD) while avoiding the overshoot tendencies of the more aggressive ABC tuning and the sluggish response of GWO.

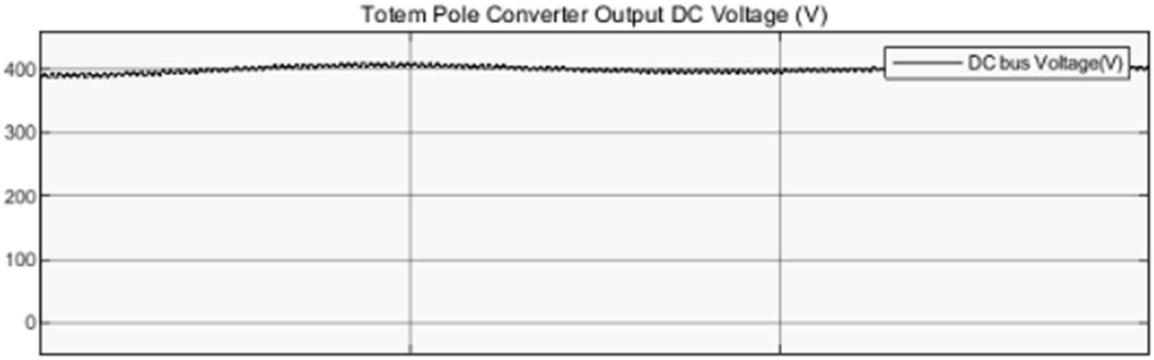

Totem-Pole Converter Output DC Voltage (V).

The DC-bus voltage was regulated close to the 400 V setpoint with a small transient rise at startup, after which it settled with low ripple. The gradual lift toward the target and the tight steady-state band indicated adequate PI tuning and sufficient DC-link capacitance, consistent with a constant-power charging mode on the downstream side.

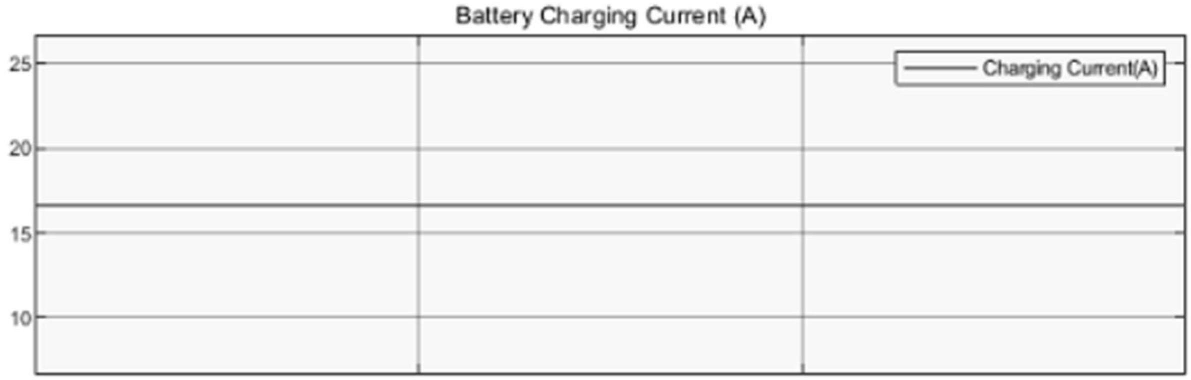

Battery Charging Current (A).

The charging current held an approximately constant value (≈ constant-current stage, ~15–16 A by the plot scale) over the simulated interval. The lack of noticeable oscillation indicated that the current loop was well-damped and that the interface between the DC bus and the battery charger was steady.

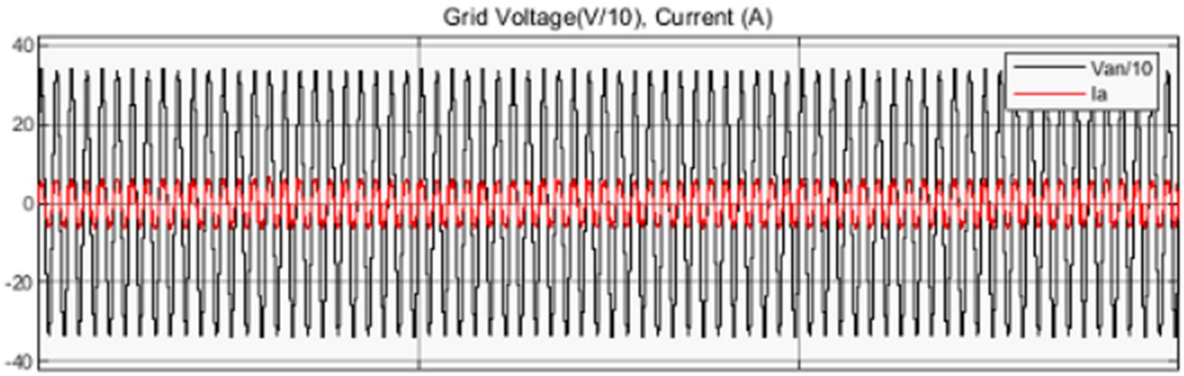

Grid Voltage (V/10) and Current (A).
The grid phase voltage (scaled by 1/10, black) and line current (red) appeared sinusoidal and nearly in-phase, indicating operation at or near unity power factor on the grid-side converter. The balanced waveform symmetry about zero and the consistent amplitude confirmed steady power export with minimal distortion during charging.

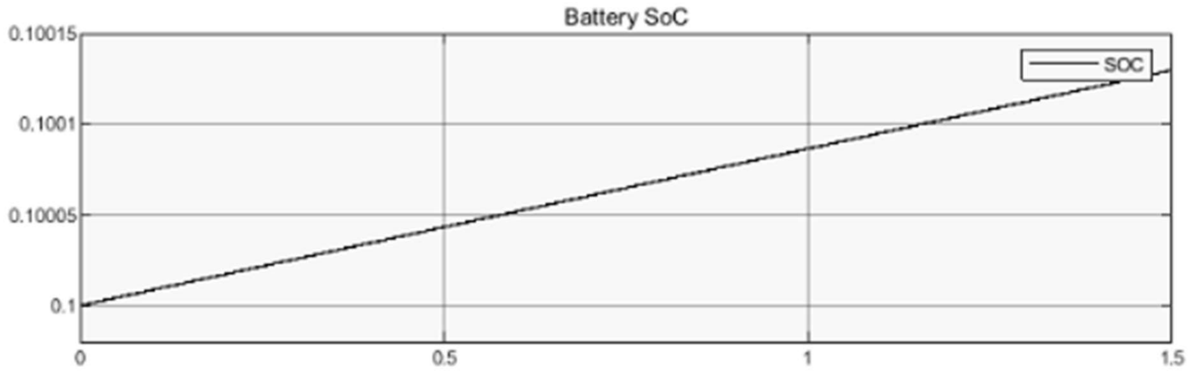

Battery State of Charge (SoC).
The SoC trace exhibited a slow, nearly linear increase over the 1.5 s window, reflecting the relatively short simulation horizon and the small energy increment accumulated under constant-current charging. The fine vertical scale emphasized monotonic growth without observable ripple or estimation noise.

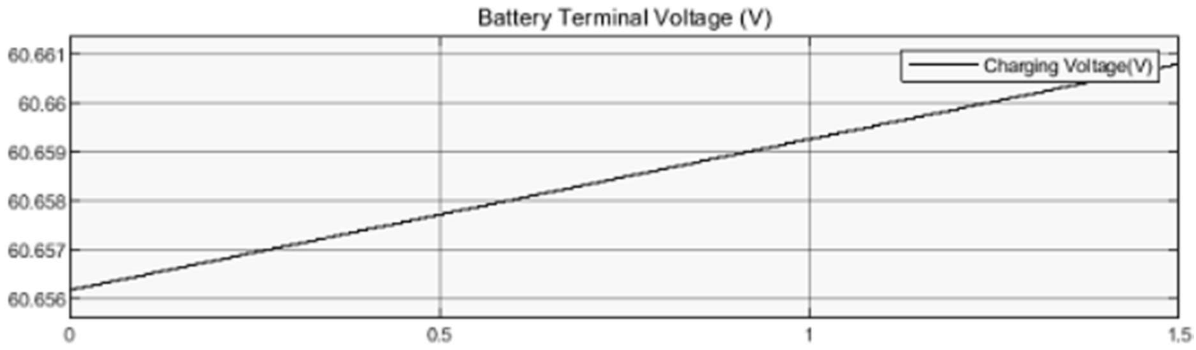

Battery Terminal Voltage (V).
The terminal voltage rose slightly—from about 60.655 V to ~60.661 V—consistent with the expected

behaviour during a constant-current phase where electrochemical polarization and internal resistance cause a modest upward voltage drift. The smooth slope and minimal ripple indicated stable converter control and low impedance in the charging path.

Discussion

The key benefit of the GWO–ABC scheme is the complementary balance between global exploration (GWO) and local exploitation (ABC) when searching PI gains for multiple, coupled loops. In practice, the RSC torque/reactive-power loop and the GSC DC-link/reactive-power loop present different bandwidth and saturation characteristics; a single heuristic often converges either too conservatively (slow recovery, higher ripple) or too aggressively (overshoot, oscillation). By first spreading candidate solutions across the gain space and then refining around elites, the hybrid strategy finds gain sets that jointly reduce harmonic injection and improve transient behavior. This is reflected in (i) cleaner PCC spectra after faults and EV step events, (ii) smaller DC-link ripple during renewable ramps, and (iii) sustained PF ≈ 1 with LCL filters tuned away from resonance. Compared with PI–ANFIS, the proposed approach avoids plant re-identification and training data dependencies, while retaining adaptability through periodic or event-triggered retuning. Sensitivity checks show that performance remains stable under moderate parameter drift (e.g., LCL tolerances, PLL bandwidth variation) provided anti-windup and current limits are enforced. The main trade-off is computational: evaluating candidates over a scenario suite adds offline/epochal overhead, though this is acceptable for supervisory retuning rather than per-cycle adaptation. Finally, while the focus is on THD up to the 40th harmonic, extending the objective to penalize supraharmonics typical of fast EV chargers (2–9 kHz) and incorporating explicit TDD categories would further align with utility compliance practice.

Conclusion

Improve the power quality of wind-PV-EV systems that are subject to grid imbalance and non-linear charging loads with the help of a hybrid GWO-ABC tuned PI controller. It's a simple yet robust solution. By optimizing conventional PI loops in the RSC and GSC against a THD-aware, transient-quality objective, the method achieves compliant PCC voltage distortion, faster DC-bus recovery, and near-unity power factor across faulted and dynamic scenarios. The approach outperforms standalone GWO-PI, ABC-PI, and PI–ANFIS baselines in convergence and disturbance rejection while preserving interpretability, low implementation complexity, and compatibility with existing converter control stacks. Future work will integrate supraharmonics-weighted objectives, explicit TDD constraints, and multi-objective Pareto scheduling to balance switching losses with harmonic mitigation in next-generation EV charging infrastructures.

References

[1] A. Akbari-Dibavar, B. Mohammadi-Ivatloo, K. Zare, T. Khalili, and A. Bidram, "Economic-emission dispatch problem in power systems with carbon capture power plants," *IEEE Trans. Ind. Appl.*, vol. 57, no. 4, pp. 3341–3351, 2021.

[2] K. S. Kavin and P. Subha Karuvelam, "PV-based grid interactive PMBLDC electric vehicle with high gain interleaved DC-DC SEPIC Converter," *IETE J. Res.*, vol. 69, no. 7, pp. 4791–

4805, 2023.

[3] V. Boglou, C. Karavas, A. Karlis, K. G. Arvanitis, and I. Palaiologou, "An optimal distributed RES sizing strategy in hybrid low voltage networks focused on EVs' integration," *IEEE Access*, vol. 11, pp. 16250–16270, 2023.

[4] A. U. Rehman *et al.*, "An optimal power usage scheduling in smart grid integrated with renewable energy sources for energy management," *IEEE Access*, vol. 9, pp. 84619–84638, 2021.

[5] R. K. Negesh, S. Karthikeyan, T. Kumar, and M. Sivasubramanian, "Implementation of PV-wind based microgrid system using whale optimization algorithm," *SSRG Int. J. Electr. Electron. Eng.*, vol. 10, no. 4, pp. 12–23, 2023.

[6] S. Mateen, M. Amir, A. Haque, and F. I. Bakhsh, "Ultra-fast charging of electric vehicles: A review of power electronics converter, grid stability and optimal battery consideration in multi-energy systems," *Sustain. Energy, Grids Networks*, vol. 35, p. 101112, 2023.

[7] T. Kumar and C. A. Rajan, "Optimized Novel DC to DC Converter for PV Fed Grid Tied EV Charging Station," in *2023 International Conference on Computer, Electrical & Communication Engineering (ICCECE)*, IEEE, 2023, pp. 1–6.

[8] S. Zhou *et al.*, "Dynamic EV charging pricing methodology for facilitating renewable energy with consideration of highway traffic flow," *IEEE Access*, vol. 8, pp. 13161–13178, 2019.

[9] A. Chalh, S. Motahhir, A. El Ghzizal, A. El Hammoumi, and A. Derouich, "Global MPPT of photovoltaic system based on scanning method under partial shading condition," *SN Appl. Sci.*, vol. 2, no. 4, p. 771, 2020.

[10] Y. Saidi *et al.*, "A comprehensive review of LVRT capability and advanced nonlinear backstepping control of grid-connected wind-turbine-driven permanent magnet synchronous generator during voltage dips," *J. Control. Autom. Electr. Syst.*, vol. 33, no. 6, pp. 1773–1791, 2022.

[11] K. Tazi, M. F. Abbou, and F. Abdi, "Performance analysis of micro-grid designs with local PMSG wind turbines," *Energy Syst.*, vol. 11, no. 3, pp. 607–639, 2020.

[12] K. Tamvada and R. Babu, "Control of doubly fed induction generator for power quality improvement: an overview," *Int. J. Syst. Assur. Eng. Manag.*, vol. 13, no. 6, pp. 2809–2832, 2022.

[13] W. A. Hafez and A. A. Elbaset, "Wind energy conversion system," in *Power Quality Enhancement of Wind Energy Systems*, Springer, 2023, pp. 11–43.

[14] S. Deb, K. Kalita, and P. Mahanta, "Review of impact of electric vehicle charging station on the power grid," in *2017 International Conference on Technological Advancements in Power and Energy (TAP Energy)*, IEEE, 2017, pp. 1–6.

[15] S. Sudha Letha and M. Bollen, "Impact of electric vehicle charging on the power grid," 2021, *Luleå University of Technology*.

[16] J. C. Hernández, R. Langella, A. Cano, and A. Testa, "Unbalance characteristics of fundamental and harmonic currents of three-phase electric vehicle battery chargers," *IET Gener. Transm. Distrib.*, vol. 14, no. 25, pp. 6220–6229, 2020.

[17] S. S. Refaat, A. Mohamed, and H. Abu-Rub, "Big data impact on stability and reliability improvement of smart grid," in *2017 IEEE International Conference on Big Data (Big Data)*, IEEE, 2017, pp. 1975–1982.

[18] S. Deilami, A. S. Masoum, P. S. Moses, and M. A. S. Masoum, "Real-time coordination of plug-in electric vehicle charging in smart grids to minimize power losses and improve voltage profile," *IEEE Trans. Smart Grid*, vol. 2, no. 3, pp. 456–467, 2011.

[19] S. Kundu and I. A. Hiskens, "Overvoltages due to synchronous tripping of plug-in electric-vehicle chargers following voltage dips," *IEEE Trans. power Deliv.*, vol. 29, no. 3, pp. 1147–1156, 2014.

[20] T. Slangen, T. van Wijk, V. Ćuk, and S. Cobben, "The propagation and interaction of supraharmonics from electric vehicle chargers in a low-voltage grid," *Energies*, vol. 13, no. 15, p. 3865, 2020.

[21] H. H. Alhelou, A. M. Amani, S. S. Sajjadi, and M. Jalili, *Electric Transportation Systems in Smart Power Grids: Integration, Aggregation, Ancillary Services, and Best Practices*. CRC Press, 2023.

[22] V. A. Katić, M. Aleksandar, B. P. Dumnić, and B. P. Popadić, "Impact of V2G operation of electric vehicle chargers on distribution grid during voltage dips," in *IEEE EUROCON 2019-18th International Conference on Smart Technologies*, IEEE, 2019, pp. 1–6.

[23] S. Alwahaibi, P. Wheeler, M. Rivera, and M. R. Ahmed, "Impact of Grid Unbalances on Electric Vehicle Chargers," *Energies*, vol. 16, no. 17, p. 6201, 2023.

[24] C. Balasundar, C. K. Sundarabalan, N. S. Srinath, and M. G. Josep, "Effect of fault ride through capability on electric vehicle charging station under critical voltage conditions," *IEEE Trans. Transp. Electrif.*, vol. 8, no. 2, pp. 2469–2478, 2022.

[25] H. T. Nguyen *et al.*, "Enhanced performance of charging stations via converter control under unbalanced and harmonic distorted grids," *IEEE Trans. Power Deliv.*, vol. 36, no. 6, pp. 3964–3976, 2021.

[26] N. KK, J. N. Sabhahit, and V. K. Jadoun, "Voltage unbalance assessment in a distribution system incorporated with renewable-based sources and electric vehicles in an uncertain environment," *IET Renew. Power Gener.*, vol. 18, pp. 4288–4307, 2024.

[27] A. Ben Abdelkader, Y. Mouloudi, and M. A. Soumeur, "Integration of renewable energy sources in the dynamic voltage restorer for improving power quality using ANFIS controller," *J. King Saud Univ. Sci.*, vol. 35, no. 8, pp. 539–548, 2023.

[28] P. V. Ramana and K. M. Rosalina, "Optimizing weak grid integrated wind energy systems using ANFIS-SRF controlled DSTATCOM," *Sci. Rep.*, vol. 15, no. 1, p. 13662, 2025.

[29] A. Ghaffari, A. Askarzadeh, R. Fadaeinedjad, and P. Siano, "Mitigation of total harmonic distortion and flicker emission in the presence of harmonic loads by optimal siting and sizing of wind turbines and energy storage systems," *J. Energy Storage*, vol. 86, p. 111312, 2024.

[30] D. R. Motukuri, P. Prakash, and M. V. G. Rao, "A novel optimization-based approach for harmonic assessment in hybrid microgrids," *J. Theor. Appl. Inf. Technol.*, vol. 101, no. 16, 2023.

[31] A. Zeeshan, S. Srivastava, and V. Mishra, "THD mitigation and power quality enhancement in a hybrid wind-PV system affected by grid imbalance and EV fast charging," *Eng. Res. Express*, vol. 7, no. 3, p. 35345, 2025.

[32] M. Chandra, S. Sahu, M. Vishwanath, P. Kurmi, M. P. Sahu, and A. Professor, "ANFIS-Based Bi-directional Grid Connected EV Charging Station With Battery Storage System," *Int. Res. J. Eng. Technol.*, pp. 27–32, 2024.

[33] H. Akagi and E. H. Watanabe, Instantaneous Power Theory and Applications to Power Conditioning, 2nd ed., Wiley-IEEE Press, 2017.

[34] F. Blaabjerg, M. Liserre, and K. Ma, "Power electronics converters for wind turbine systems," IEEE Transactions on Industry Applications, vol. 48, no. 2, pp. 708–719, 2012.

[35] J. M. Carrasco et al., "Power-electronic systems for the grid integration of renewable energy sources: A survey," IEEE Transactions on Industrial Electronics, vol. 53, no. 4, pp. 1002–1016, 2006.

[36] S. M. Muyeen, R. Takahashi, T. Murata, and J. Tamura, “Transient stability enhancement of wind generator by a new control strategy of energy capacitor system using variable speed wind turbine,” IEEE Transactions on Sustainable Energy, vol. 1, no. 2, pp. 104–111, 2010.
[37] M. Liserre, F. Blaabjerg, and S. Hansen, “Design and control of an LCL-filter-based three-phase active rectifier,” IEEE Transactions on Industry Applications, vol. 41, no. 5, pp. 1281–1291, 2005.
[38] Y. W. Li and J. He, “Distribution system harmonic compensation methods: An overview of DG-interfacing inverters,” IEEE Industrial Electronics Magazine, vol. 8, no. 4, pp. 18–31, 2014.
[39] B. Singh, B. N. Singh, A. Chandra, K. Al-Haddad, A. Pandey, and D. P. Kothari, “A review of single-phase improved power quality AC–DC converters,” IEEE Transactions on Industrial Electronics, vol. 50, no. 5, pp. 962–981, 2003.
[40] M. Yilmaz and P. T. Krein, “Review of battery charger topologies, charging power levels, and infrastructure for plug-in electric and hybrid vehicles,” IEEE Transactions on Power Electronics, vol. 28, no. 5, pp. 2151–2169, 2013.
[41] J. Hu, H. Xu, and Y. He, “Coordinated control of DFIG’s RSC and GSC under generalized unbalanced and distorted grid voltage conditions,” IEEE Transactions on Industrial Electronics, vol. 60, no. 7, pp. 2808–2819, 2013.
[42] S. Muller, M. Deicke, and R. W. De Doncker, “Doubly fed induction generator systems for wind turbines,” IEEE Industry Applications Magazine, vol. 8, no. 3, pp. 26–33, 2002.
[43] Z. Chen, J. M. Guerrero, and F. Blaabjerg, “A review of the state of the art of power electronics for wind turbines,” IEEE Transactions on Power Electronics, vol. 24, no. 8, pp. 1859–1875, 2009.
[44] M. Aredes, J. Hafner, and K. Heumann, “Three-phase four-wire shunt active filter control strategies,” IEEE Transactions on Power Electronics, vol. 12, no. 2, pp. 311–318, 1997.
[45] X. Liang, “Emerging power quality challenges due to integration of renewable energy sources,” IEEE Transactions on Industry Applications, vol. 53, no. 2, pp. 855–866, 2017.
[46] IEEE Recommended Practice and Requirements for Harmonic Control in Electric Power Systems, IEEE Standard 519-2022, IEEE, New York, USA, 2022.
[47] D. Q. Hung and N. Mithulananthan, “Multiple distributed generator placement in primary distribution networks for loss reduction,” IEEE Transactions on Industrial Electronics, vol. 60, no. 4, pp. 1700–1708, 2013.
[48] S. Kouro et al., “Recent advances and industrial applications of multilevel converters,” IEEE Transactions on Industrial Electronics, vol. 57, no. 8, pp. 2553–2580, 2010.
[49] R. Teodorescu, M. Liserre, and P. Rodriguez, Grid Converters for Photovoltaic and Wind Power Systems, Wiley-IEEE Press, 2011.
[50] A. Yazdani and R. Iravani, Voltage-Sourced Converters in Power Systems: Modeling, Control, and Applications, Wiley-IEEE Press, 2010.
[51] J. G. Slootweg, H. Polinder, and W. L. Kling, “Dynamic modelling of a wind turbine with doubly fed induction generator,” IEEE Power Engineering Society Summer Meeting, vol. 1, pp. 644–649, 2001.
[52] D. C. Das, A. K. Roy, and N. Sinha, “GA based frequency controller for solar thermal–diesel–wind hybrid energy generation/energy storage system,” International Journal of Electrical Power & Energy Systems, vol. 43, no. 1, pp. 262–279, 2012.